Original Article

The impact of Adjustable-Ring-Mode (ARM) laser beam on the microstructure and mechanical performance in remote laser welding of high strength aluminium alloys

Tianzhu Sun [a,*], Anand Mohan [a,**], Conghui Liu [b], Pasquale Franciosa [a], Dariusz Ceglarek [a]

[a] Warwick Manufacturing Group (WMG), University of Warwick, Coventry CV4 7AL, UK
[b] School of Materials, The University of Manchester, Manchester, M13 9PL, UK

ARTICLE INFO

ABSTRACT

This paper introduced the use of an adjustable-ring-mode (ARM) laser beam to optimise the microstructure and mechanical performance of laser welded 6xxx high-strength aluminium alloy joints. A remote laser welding system equipped with transverse beam oscillation was employed and welding parameters, including the beam oscillation width and core/ring power ratio of the ARM laser beam, were investigated sequentially. Results showed that the core/ring power ratio at a constant total power has a limited control on the weld geometry when integrated with beam oscillation. Increasing the beam oscillation width, up to 2.5 mm, resulted in a wider weld interface and a threshold value of 3.1 mm was determined to activate the transition from interface failure to the fusion boundary failure subjected to tensile lap shear loading, leading to a significant improvement in the joint strength from 170 N/mm to 277 N/mm. Furthermore, results revealed that proper selection of core/ring power ratio at a constant total power can restrict the formation of columnar grains near the interface between two plates, resulting in grain refinement within the weld zone. Both extremely high power ratio, for example core alone mode (infinite power ratio) and extremely low power ratio, e.g. ring alone mode (zero power ratio), lead to a low thermal gradient and cooling rate at the solidification front. A compromised solution which balances the wider formation of equiaxed dendrites and better grain refinement was determined at the power ratio of 0.33, translating to the improvement in joint strength up to 400 N/mm.

Nomenclature

ARM	Adjustable-ring-mode
OCT	Optical coherence tomography
EBSD	Electron backscatter diffraction
d_c	Diameter of the core beam at the focus plane (μm)
d_r	Diameter of the ring beam at the focus plane (μm)
S_x	Welding speed (mm·s^{-1})
A_y	Transverse oscillation width (mm)
P_c	Power of core beam (kW)
P_r	Power of ring beam (kW)
D	Grain size represented by the equivalent diameter of the circle with an area equal to the grain (μm)
$\overline{D}$	Area-weighted mean grain size (μm)
FEM	Finite element method
ρ	Density (kg·m^{-3})
u	Fluid velocity (mm·s^{-1})
η	Dynamic viscosity (Pa·s)
T	Temperature (K)
T_0	Room temperature (K)
λ	Thermal conductivity (W·mm^{-2}·K^{-1})
C_P	Specific heat capacity of the material (J·kg^{-1}·K^{-1})
Q_{laser}	Energy input per unit volume of the laser heat source (J·m^{-3})
Q_{vap}	Energy loss due to evaporation of the material
C	Mushy zone constant related to the morphology of the porous media
F	Momentum source term
β	Volume expansion coefficient
$T_{melting}$	Melting temperature
f_l	Fraction of liquid
T_L	Liquidus temperature of materials
T_S	Solidus temperature of materials
$C_{p,S}$	Heat capacity of the solid phase (J·kg^{-1}·K^{-1})
$C_{p,L}$	Heat capacity of the liquid phase (J·kg^{-1}·K^{-1})
Q_{core}	Heat input of the core beam
Q_{ring}	Heat input of the ring beam
H	Heat source height (mm)
α	Absorption coefficient of the material
Q_f	Power density in the front quadrant of the double ellipsoid heat source (J·m^{-3})
Q_r	Power density in the rear quadrant of the double ellipsoid heat source (J·m^{-3})
h	Convection coefficient (W·m^{-2}K^{-1})
ε	Material's optical emissivity
σ	Stefan-Boltzman constant
L_v	Latent heat of vaporisation (J·kg^{-1})
W_I	Weld interface width (mm)
W_T	Weld top width (mm)

1.   Introduction

Automotive sectors are increasingly pursuing 6xxx series aluminium alloys because of the high strength-to-weight ratio,

excellent formability and good corrosion resistance [1]. The active response of 6xxx series aluminium alloys to strengthening processes including thermal treatment and work hardening provides the opportunity for weight saving without compromising the strength. This is particularly crucial for battery electric vehicles (BEVs) as it allows for downsizing the battery system and reducing costs [2]. Remote laser welding (RLW) is emerging as a lightweight solution to material joining in automotive applications due to the abandonment of filler wire and shielding gas. In addition, it brings benefits such as remarkable processing efficiency and flexibility, gained from the rapid weld-to-weld repositioning and non-contact single-side access [3,4]. However, laser welding of aluminium alloys is challenged by the low energy efficiency and high susceptivity to weld defects because of the high reflectivity, high thermal expansion rate and low viscosity [5−7].

Optimising the chemical composition in the fusion zone is a well-studied metallurgical approach to improving the performance of laser welds, for example, the selection of proper filler material during the conventional laser welding process [8]. Concerning the nature of the RLW process where no filler wire is used, the addition of alloying elements to the base material [9] and utilisation of multi-layer base material [10] have been reported alternatively. Recently, researchers proposed the beam oscillation technique as a thermal approach to improving the weld performance by modifying the weld thermal cycle [11], which is enabled by the scanning welding head and can be fully integrated into the RLW process, providing flexibility in defining spatial energy distribution within the weld zone. Wang et al. [12] demonstrated that the oscillating laser beam promotes the formation of equiaxed grains and break-up of the columnar dendrites due to a more uniform temperature distribution and mechanical stirring effect in the molten pool. Fetzer et al. [13] experimentally reported the reduction of weld porosity by utilising laser beam oscillation, which was further confirmed by Li et al. [14] with numerical simulation. Li et al. also proposed that circular oscillation is more effective than transverse oscillation and non-oscillation due to the lowest melt flow velocity and the most complicated vortices in the molten pool. In addition, Zhang et al. [15] claimed that increasing the oscillation width and frequency can result in more significant mitigation of weld porosity and consequently higher joint strength.

More recently, the beam shaping technique, which enables the tuning of beam shape and size directly from the feeding fibre, was proposed as an additional thermal approach to improve welding performance [16]. Rasch et al. [17] and Duocastella and Arnold [18] reported the benefits of ring shape laser beam for stabilising the molten pool and improving the weld surface quality. However, a conduction mode laser welding is generally observed in these studies and the lack of weld penetration prohibited the application of ring beam for joining thick materials. Subsequently, Coherent Inc introduced the adjustable-ring-mode (ARM) laser beam [19], consisting of an inner spot beam and an outer ring beam. Under this beam configuration, pre-heating supplied by the leading edge of the ring beam increases the material's energy absorption rate and the post-heating enabled by the trailing edge of the ring beam enlarges the molten pool to promote the escape of gas bubbles, whilst the core beam guarantees a

sufficient weld penetration. The benefits of ARM laser beams have been reported in a limited number of studies. Maina et al. [19] demonstrated the improvements in both surface quality and keyhole stability in AA5022 laser welds using an ARM laser beam compared to the sole annular laser beam. Mohammadpour et al. [20] experimentally studied ARM laser welding of stainless steel and reported a noticeable spatter reduction on the weld bead at a power ratio of the core beam to a ring beam of less than one. Sokolov et al. [21] investigated the impact of ARM laser on the in-process weld penetration monitoring by optical coherence tomography (OCT) during RLW of Al–Cu dissimilar thin foil. The authors observed a reduced fluctuation of keyhole opening and reported that the ARM laser beam allowed a 50% improvement in the accuracy of OCT compared to the Gaussian laser beam. Despite the aforementioned advantages of the ARM laser beam, predominantly focusing on the process stability and seam surface finish, the impact of the ARM laser beam on the weld microstructure and mechanical performance is still unclear.

This paper aims to explore the capability of new emerging laser technology for E-mobility manufacturing by investigating the impact of the Adjustable Ring Mode laser beam on the weld microstructure and mechanical performance of 6xxx series aluminium alloy lap joints. A remote laser welding system equipped with transverse beam oscillation and ARM laser source was employed. Beam oscillation width and core/ring power ratio of the ARM laser beam were evaluated sequentially. The geometry of the weld was determined by optical microscopy and weld zone grain morphology was determined by electron backscatter diffraction (EBSD). Furthermore, the mechanical performance of welds was characterised by the tensile lap shear test along the transverse direction. A coupled three-dimensional heat transfer and fluid flow model was developed to investigate the effect of core/ring power ratio on the thermal history and provide insight into the resultant solidification microstructure.

2. Experimental details

The material studied in this paper belongs to the 6xxx series aluminium alloy in the T6 temper. Plates were machined into the size of 100 mm (length) × 45 mm (width) × 3 mm (thickness) and cleaned with acetone to remove surface contaminations prior to welding. A lap joint configuration with an overlap length of 20 mm was employed, as schematically illustrated in Fig. 1(a). To avoid heat sinking, a slot with a width of 15 mm was machined in the backplate and located well beneath the weld seam. No shielding gas or filler wire was used throughout.

A 10 kW ARM fibre laser source (HighLight FL10000-ARM, Coherent), 5 kW for core beam and 5 kW for ring beam, was employed and delivered by Precitec YW52 remote welding head with a collimating length of 150 mm and focal length of 300 mm. A glass material with a low refraction index is designed to isolate the core and ring beam [19]. Fibres with a diameter of 70 μm for the core beam and 180 μm for the ring beam diameter were utilised, which leads to the diameter at the focus of 140 μm for the core beam (d_c) and 360 μm for the ring beam (d_r), respectively, as shown in Fig. 1(a).

During welding, the welding head was tilted at 10° from the vertical direction (z-axis) to reduce the potential risk of back-reflection and the laser beam was focused on the top surface of the upper part at 10 mm (along the y-axis) from the edge of the free side, as illustrated in Fig. 1(a). Constant welding speed (S_x) of 50 mm/s and the transverse oscillation frequency of 50 Hz was adopted throughout all welding trials. The matrix of studied welding parameters, including transverse oscillation width (A_y) and core/ring power ratio (P_c/P_r) is summarised in Table 1. Several welding trials were initially conducted to determine the optimised beam oscillation width concerning the joint strength. The optimised A_y was subsequently employed to investigate the impact of power ratios on the weld microstructure and mechanical strength. It should be noted that the total power in the study of power ratio was increased by 0.75 kW compared to weld trials for the pre-selection of A_y to allow sufficient bonding between the two plates over a wide range of power ratios. Theoretical Intensity profiles of the ARM laser at the focus plane with different power ratios with a constant total power of 6 kW are visualised in Fig. 2.

The welded samples were sectioned normal to the welding direction and polished to a 0.06 μm surface finish, followed by etching in caustic sodium fluoride reagent (2% NaOH + 5%NaF + 93% water). The weld geometry was determined using Keyence VHX7000 optical microscope along the transverse (y-z) cross-section. Weld zone grain structure was characterised by EBSD mapping on unetched samples with additional vibratory polishing in colloidal silica suspension for 3 h. EBSD was conducted on a JEOL 7800F scanning electron microscope, equipped with an Oxford Instruments' Symmetry II EBSD detector and AZtec acquisition software with an accelerating voltage of 20 kV and a step size of 3 μm. Grain size (D) is represented by the equivalent diameter of the circle with an area equal to the grain. An area-weighted mean value, $\overline{D} = \frac{\sum W_i D_i}{\sum W_i}$ was used to express the averaged grain size within the weld zone considering the significant scatter of individual grain size between the columnar grains and equiaxed grains after solidification. Tensile lap shear tests were conducted along the transverse direction at a constant extension rate of 1 mm/min, following ISO standards [22] on Instron® 3360 tensile machine equipped with the 30 kN load cell, Fig. 1(b). Specimens for the tensile test had an effective weld seam length of 20 mm and tests were repeated four times at each welding condition. The mechanical strength of the welded structure was evaluated by the maximum load (kN) from the load-strain curve. It should be noted that tensile tests were conducted after post-weld natural ageing for one month.

3. Numerical simulation

To understand the evolution of thermal history as a function of the power ratio of ARM laser, a transient three-dimensional numerical model is developed based on the finite element method (FEM). A volumetric hybrid heat source is employed to model the heat distribution from the laser to the workpiece. A three-dimensional cartesian system is utilised where the x-axis is defined as the laser head moving direction, the y-axis is
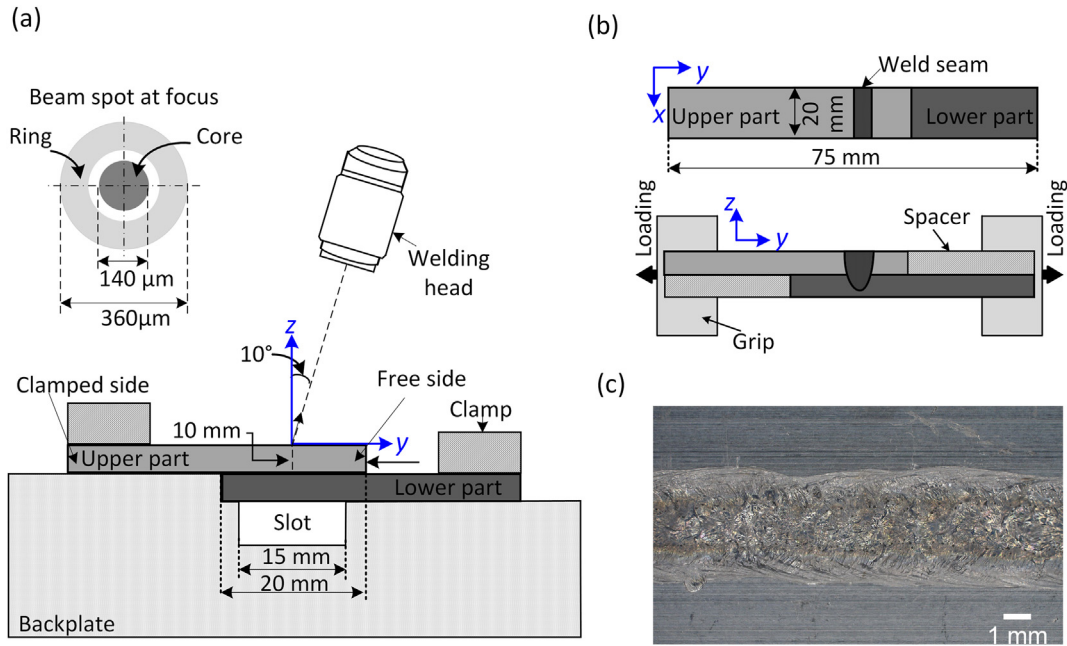
Fig. 1 − Schematic diagram showing experimental set-up for (a) welding test with the ARM laser beam and (b) specimen geometry and tensile lap shear tests, and (c) representative top view of the weld.

defined as the weld cross-section direction along the width of the workpiece, and the z-axis is defined as the direction of weld penetration. The oscillating laser beam is composed of two types of motions in the x-y plane: a sinusoidal motion and a linear forward motion in the welding direction. Following assumptions are made to improve the efficiency of the calculation without affecting the accuracy: (a) the liquid metal formed is considered Newtonian and incompressible, and fluid flow is considered laminar; (b) Boussinesq's approximation is used to account for the change of density due to temperature variations [23]; (c) the surface of weld pool formed is considered flat and keyhole dynamics are not considered to simplify the model and decrease the computational time, whereas a volumetric heat source model is used to replicate keyhole which is a common practice as evidenced by [23–28]; (d) temperature-dependent material properties are considered; (e) no vapour and plasma flow is considered in the simulation; (f) the absorption of laser energy by the workpiece is kept constant which is assumed to be independent of temperature changes; (g) the laser absorption coefficient is kept the same for the ring and the core.

3.1. Governing equations

The governing equations of conservation of energy, mass, and momentum for describing the heat transfer and fluid flow during laser welding are expressed as [23]:

Energy conservation

$$\rho C_P \frac{\partial T}{\partial t} + \rho C_P u \bullet \nabla T = \nabla \bullet (\lambda \nabla T) + Q_{laser} + Q_{vap} \tag{1}$$

Mass conservation

$$\nabla \bullet u = 0 \tag{2}$$

Momentum conservation

$$\rho \frac{\partial(u)}{\partial t} = -\rho(u \bullet \nabla u) - \nabla P + \eta(\nabla^2 u) + F \tag{3}$$

where ρ is the density, t is the time, u is the fluid velocity, η is the dynamic viscosity, P is the pressure, T is the temperature, λ is the thermal conductivity, C_P is the specific heat capacity of the material, Q_{laser} is the energy input per unit volume of the laser heat source and Q_{vap} is the energy loss due to

Table 1 − Matrix of welding parameters studied in this paper.			
Pre-selection of Beam Oscillation Width			
Oscillation width A_y (mm)	0; 0.5; 1.5; 2.5; 3.5	Power of core beam P_c (kW)	3.25
Power of ring beam P_r (kW)	2.00	Power ratio P_c/P_r	1.63
Study of Power Ratio			
Oscillation width A_y (mm)	2.5;	Power of core beam P_c (kW)	1.00; 1.50; 2.00; 2.50; 3.50;
Power of ring beam P_r (kW)	5.00; 4.50; 4.00; 3.50; 2.50;	Power ratio P_c/P_r	0.20; 0.33; 0.50; 0.71; 1.40
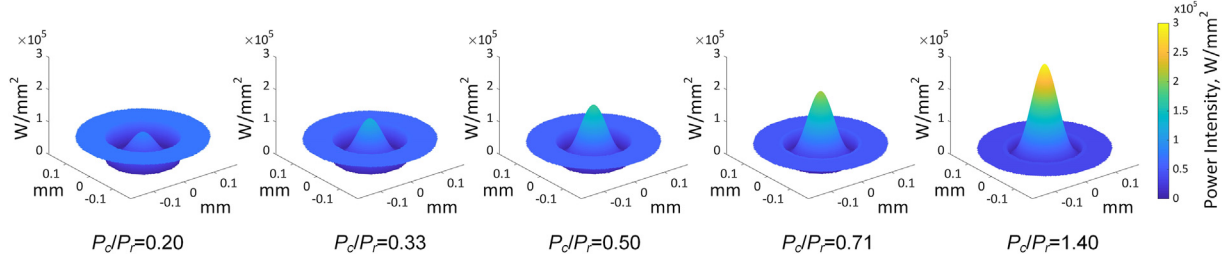
Fig. 2 − Theoretical Intensity profiles of ARM laser at focus plane with different power ratios with a constant total power of 6 kW.

evaporation of the material, F is the momentum source term which is defined as follows [29]:

$$F = C\left(-\frac{(1-f_l)^2}{f_l^3 + B} \right)u + \rho g\beta(T - T_{melting}) \tag{4}$$

The first term on the right-hand side of Eq. (4) is according to the Carman-Kozeny equation for flow through a porous media [26,30], representing the frictional dissipation which ensures a smooth transition of velocity from zero to a large value in the mushy zone; B is a merely computational constant, very small positive number to avoid division by zero is set at 0.001; C is a mushy zone constant related to the morphology of the porous media, which is a large number (a value of 1.6×10^4 was used in the present study) to force the velocity of the solid zone to be zero and represents mushy zone morphology; β is the coefficient of volume expansion; g is the acceleration due to gravity; $T_{melting}$ is the melting temperature which is average of solidus and liquidus temperature, and f_l is the fraction of liquid defined in Eq. (5), where, T_L and T_S are liquidus and solidus temperature of the materials, respectively. The second term on the right-hand side of Eq. (4) accounts for the natural convection.

$$f_l = \begin{cases} 1 & T > T_L \\ \frac{T - T_S}{T_L - T_S} & T_S \leq T \leq T_L \\ 0 & T < T_S \end{cases} \tag{5}$$

The phase changes from solid and liquid are considered to include temperature change due to latent heat by using the apparent heat capacity method which includes an additional term for latent heat as shown in Eq. (6)

$$C_P = C_{P,S}.(1 - f_l) + C_{P,L}.f_l + \frac{H_m}{\Delta T}f_l \tag{6}$$

where, $C_{p,S}$ is the heat capacity of the solid phase, $C_{p,L}$ is the heat capacity of the liquid phase, H_m is the melting latent heat.

3.2. Heat source model

The general trajectory of the moving laser beam is given in Eq. (7) where (x_0, y_0, z_0) is the origin, S_x is the welding speed, A is the oscillation amplitude which is half of the oscillation width (A_y), and f is the oscillation frequency.

$$(x_{(t)}, y_{(t)}, z_{(t)}) = (x_0 + S_x t, \ y_0 + A\sin(2\pi ft), \ z_0) \tag{7}$$

To include beam inclination as illustrated in Fig. 1, the trajectory of the laser beam can be further determined as:

$$\begin{cases} x' = x_{(t)} \\ y' = \cos(a)(y - y_{(t)}) - \sin(a)(z - z_{(t)}) \\ z' = \cos(a)(z - z_{(t)}) - \sin(a)(y - z_{(t)}) \end{cases} \tag{8}$$

Where a is the angle of inclination, x', y' and z' are the co-ordinates of the laser beam after the inclination.

The total heat input to the workpiece is the summation of energy absorbed by the core and the ring part of the laser as given in Eq. (9) where Q_{core} is the heat input by the core beam and Q_{ring} is the heat input by the ring beam.

$$Q_{laser}(x, y, z, t) = Q_{core}(x, y, z, t) + Q_{ring}(x, y, z, t) \tag{9}$$

Since the core beam has a very high power density as compared to the ring beam, it is assumed that the core beam affects the penetration of the laser beam and the ring beam affects the surface and near-surface thermal field. Consequently, the core beam is modelled using a volumetric heat source and the ring beam is modelled using a surface heat flux.

The core beam is simulated as a hybrid volumetric heat source consisting of a double ellipsoid heat source [31] and a rotating Gauss body heat source [15,28] and is expressed as:

$$\begin{aligned} &Q_f(x, y, z, t) \\ &= \alpha \frac{6\sqrt{3}f_f P_c}{a_f bc\pi\sqrt{\pi}} exp\left(-3\frac{(x - x')^2}{a_f^2} - 3\frac{(y - y')^2}{b^2} - 3\frac{(z - z')^2}{c^2} \right) \end{aligned} \tag{10}$$

$$\begin{aligned} &Q_r(x, y, z, t) \\ &= \alpha \frac{6\sqrt{3}f_r P_c}{a_r bc\pi\sqrt{\pi}} exp\left(-3\frac{(x - x')^2}{a_r^2} - 3\frac{(y - y')^2}{b^2} - 3\frac{(z - z')^2}{c^2} \right) \end{aligned} \tag{11}$$

$$Q_{rg}(x, y, z, t) = \alpha \frac{9f_2 P_c}{\pi r_c^2 H(1 - e^{-3})} exp\left(-9\left(\frac{(x - x')^2 + (y - y')^2}{r_c^2 \log(H/z')} \right) \right) \tag{12}$$

$$Q_{core}(x, y, z, t) = Q_f(x, y, z, t) + Q_r(x, y, z, t) + Q_{rg}(x, y, z, t) \tag{13}$$

where P_c is the power of the core beam, r_c is the spot radius of the core, H is the heat source height, α is the absorption co-efficient of material which is taken as 0.6 [32], $Q_f(x,y,z,t)$ and $Q_r(x,y,z,t)$ are the power densities in the front and rear quadrant of the double ellipsoid heat source (Eqs. 10 and 11). The effective heat absorbed by the hybrid heat source, $Q_{rg}(x, y, z, t)$

i.e., double ellipsoid and rotating Gauss body heat source is given by Eq. (13). f_1 and f_2 are the weighting coefficients of the rotating Gauss body heat source and double ellipsoid heat source which follows $f_1 + f_2 = 1$. f_f and f_r are the weighting coefficients of the front and rear quadrant of an ellipsoid which follows $f_f + f_r = 2$, and in this study, it is set as 0.4 and 1.6 respectively. a_r, a_f, b, c are the heat source distribution parameters that depend on the size and shape of the weld pool.

The ring beam is simulated as surface heat flux in the top-hat mode and expressed in Eq. (14)

$$Q_{ring}(x, y, z, t) = \frac{\alpha P_r}{\pi(r_o^2 - r_i^2)} \tag{14}$$

Where P_r is the power of the ring beam, r_o and r_i are the outer and inner radius of the ring, respectively.

3.3. Boundary conditions

The initial temperature of the workpiece is assumed to be maintained at room temperature (T_0). The heat loss at the top and bottom surfaces due to convection, radiation and evaporation is given in Eq. (15).

$$-\lambda \nabla T = h(T - T_0) + \varepsilon\sigma(T^4 - T_0^4) + Q_{vap} \tag{15}$$

Where h is the convection coefficient, ε is the material's optical emissivity, σ is the Stefan-Boltzman constant and $Q_{vap} = WL_v$, W is the evaporation rate and L_v is the latent heat of vaporisation. Flow condition for the free liquid surface due to the surface tension gradient due to variations in temperature is given as in Eqs. 16 and 17 and the velocity along the z-direction is zero.

$$-\eta \frac{\partial u_x}{\partial z} = \frac{\partial\gamma}{\partial T}\frac{\partial T}{\partial x} \tag{16}$$

$$-\eta \frac{\partial u_y}{\partial z} = \frac{\partial\gamma}{\partial T}\frac{\partial T}{\partial y} \tag{17}$$

3.4. Calculation domain and numerical implementation

The simulations were performed using COMSOL Multiphysics 6.0 software. The algebraic multigrid (AMG) solver was adopted as it provides robust solutions for large CFD simulations. For problems solved for space and time, discretisation in space is done using the finite element method and time is discretised using the backwards differential formula (BDF). The damped Newton method is used to solve a fully coupled system of non-linear equations and the generalised minimal residual (GMRES) method is used to solve fluid flow.

The simulation domain for a single plate has a geometry of 100 mm × 50 mm × 3 mm. Each plate has been divided into five domains to improve mesh distribution having very fine mesh at the weld centerline, fine mesh at fusion zone and coarser mesh at the base metal as shown in Fig. 3. The mesh was finer for the upper plate where the laser beam is deposited as compared to the bottom plate to reduce the computation time. Mesh sensitivity analysis was conducted based on both temperature and fluid flow velocity before finalizing the mesh size and distribution. Tetragonal mesh with linear interpolation is used with a total of 1550639 mesh elements having degrees of freedom at 1679454. At the weld centerline, the minimum mesh size is $r/2$ which is 35 μm, maximum mesh size is $2r$ having maximum element growth rate of 1.05 with curvature factor 0.2 is used. At the fusion zone, the minimum mesh is r, maximum mesh size is $5r$ having maximum element growth rate of 1.02 with curvature factor 0.2 and at the base metal minimum mesh size is 830 μm having maximum element growth rate of 1.13 with curvature factor of 0.5. No gaps between plates are considered. The main material properties of the studied material are listed in Table 2 calculated from JMatPro.

4. Results and discussion

4.1. Pre-selection of beam oscillation width

Weld cross-sections at different oscillation widths were shown in Fig. 4(a), and the evolution of fusion zone geometry, e.g., weld interface width (W_I) and weld penetration (P), was summarised in Fig. 4(b) and (c). Results show that a higher oscillation width can effectively increase weld interface width but reduce weld penetration. In addition, an excessive oscillation width, i.e., $A_y = 3.5$ mm, leads to an unbonded area in the weld centre as highlighted and consequently reduces the effective weld interface width. The evolution of weld geometry is closely related to the change in laser energy distribution. With the transverse oscillation, peak laser energy density is redistributed at two turning points of the oscillating path instead of the weld centre (as seen in the case of non-oscillation ($A_y = 0$)). Furthermore, as the oscillation width increases, the energy deposited field is more spread but with a mitigated intensity due to the fixed total input power.

The evolution of joint strength in response to the beam oscillation width was investigated by tensile lap shear tests along the transverse direction and demonstrated in Fig. 5(a). An improvement of the maximum linear load from 170 N/mm to 275 N/mm can be gained by increasing the beam oscillation width, which is essentially related to the enhanced weld interface width. Failure position was determined within the fusion zone for all tests as shown in Fig. 5(b) and two failure modes were identified i.e., interface failure and fusion boundary failure. For the overlap joint configuration, stress concentration under tensile shear loading initiates at the fusion boundary near faying surface between two plates and predominantly develops the shortest path [34]. Therefore, the transition of failure mode at $W_I \geq 3.1$ mm results from the fact that the shortest path for the accommodation of stress concentration diverts into the through-thickness direction instead of the width interface direction. Similar observations were also reported in [34,35]. In addition, the fractography in Fig. 5(c) confirms the presence of an unbonded region at an excessive oscillation width, which reduces the effective weld interface width and, resultantly, the joint strength. Therefore, an optimised A_y of 2.5 mm was determined for studying the effect of power ratio of ARM laser in the following sections.
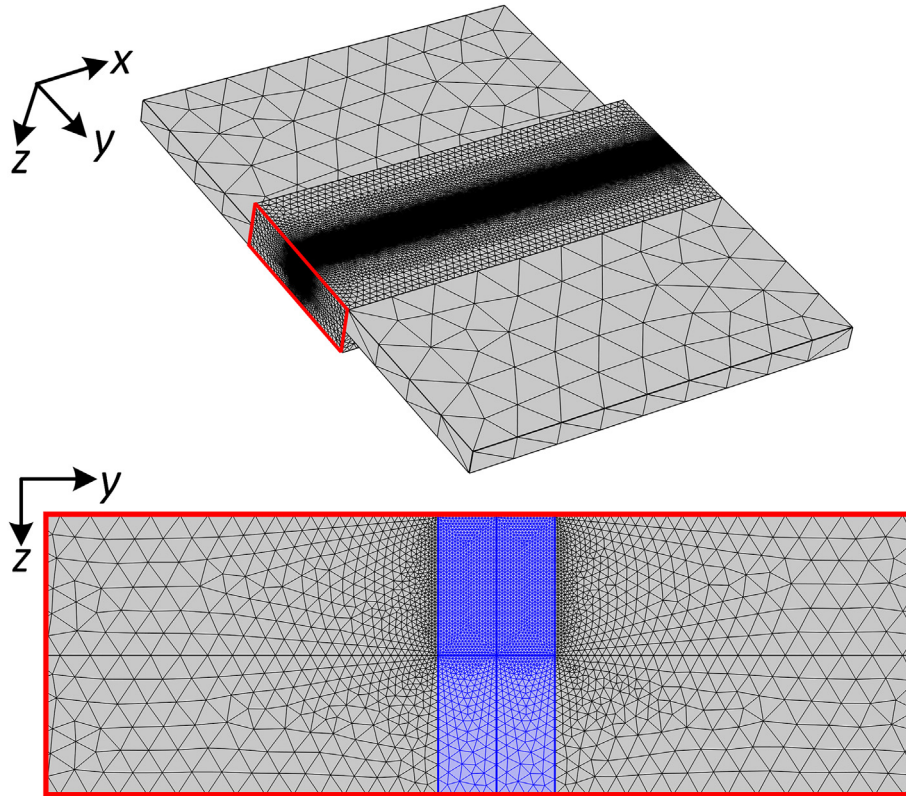
Fig. 3 – Schematic illustration of modelling domain and mesh distribution used for the simulation.

4.2. Effect of power ratio on the weld geometry

Fig. 6 shows optical cross-sections of welds produced at different core/ring power ratios. Overall, a slight reduction of weld interface width and a minor increase in weld penetration were determined when a higher portion of power was assigned to the core beam. In addition, it is clear that the variation of weld geometry resulting from different power ratios is significantly reduced compared to the case with various beam oscillation widths, as indicated by the grey area.

## 4.3. Effect of power ratio on the temperature field

A steep thermal gradient and rapid solidification behaviour of the molten material are generally expected in the laser welding process, it is challenging to obtain accurate evolution of the position-sensitive and time-sensitive temperature fields by direct experimental measurement. Therefore, numerical simulation was developed to reconstruct the temperature field and provide insight into the impact of power ratio on the mechanism of microstructural formation. The model was first evaluated using the welding trials with different oscillation widths listed in Table 1 due to a more significant variation in weld geometry, followed by the welding trials with different power ratios. Fig. 7 shows the evolution of weld geometry in terms of weld top width and weld penetration. It is evident that the simulated weld profiles are in good agreement with experimental observation, with the correlation coefficient of 0.94 and 0.95 for weld width and weld penetration, respectively, demonstrating the validity of the employed model.

Fig. 8 shows the evolution of temperature fields at steady-state as a function of power ratio, simulated by the validated model. The yellow dashed line indicates the position of the laser beam along the welding direction, and the molten pool boundary was expressed by the solid white line using the isotherm $T = (T_L + T_S)/2 = 873$ K, where T_L and T_S are the liquidus temperature and solidus temperature, respectively.

| Table 2 – Material properties of the studied material calculated by JMatPro [33].			
Density of solid (kg·m^{-3})	2695 (293 K)	Density of liquid (kg·m^{-3})	2389
Specific heat of solid (J·kg^{-1}·K^{-1})	903 (293 K)	Specific heat of liquid (J·kg^{-1}·K^{-1})	0.00117 (923 K)
Viscosity (Pa·s)	0.0013 (923 K)	Solidus (K)	823
Surface tension (N·m^{-1})	0.82 (923 K)	Liquidus (K)	923
Thermal conductivity (W·mm^{-2}·K^{-1})	207 (293 K)	Latent heat of fusion (J·kg^{-1})	3.96E+5
Convection coefficient (W·m^{-2}K^{-1})	20	Emissivity	0.3
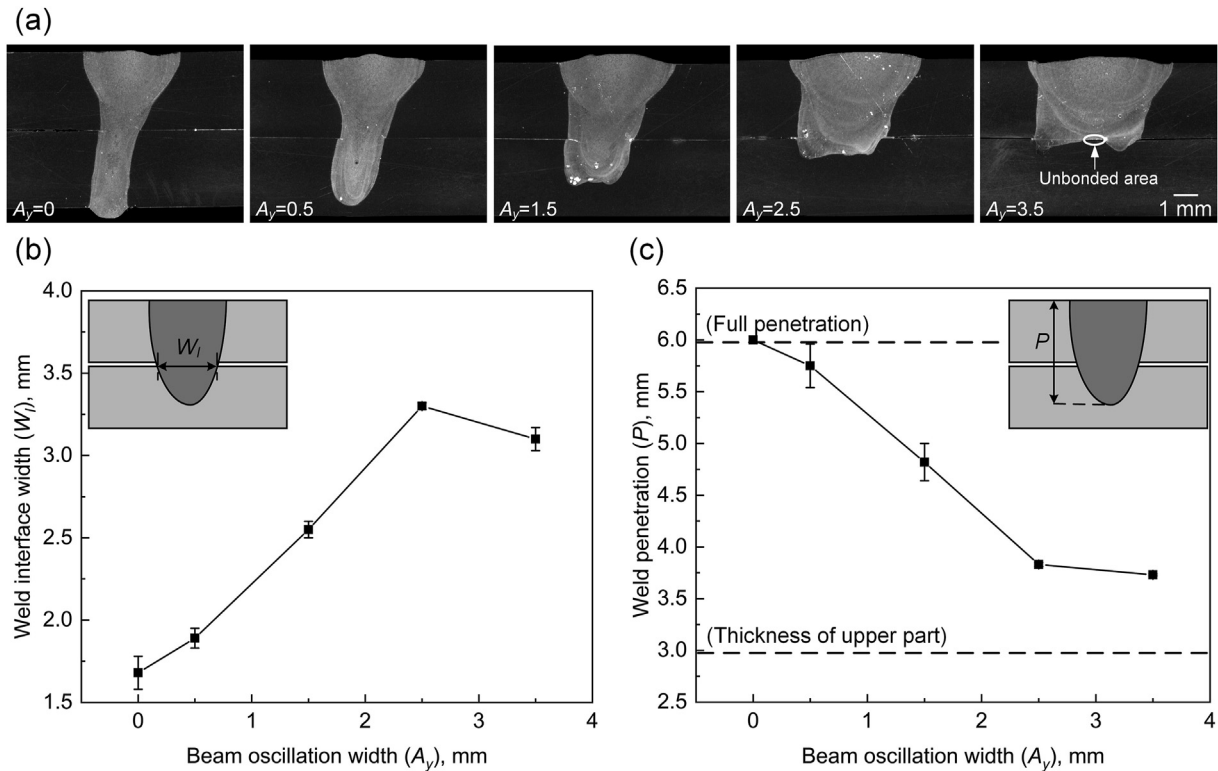
Fig. 4 − (a) Cross-section morphology of welds produced with different oscillation widths at the power of $P_c = 3.25$ kW, and $P_r = 2$ kW, and evolution of weld geometry: (b) weld interface width (W_I) and (c) weld penetration (P).

Overall, a higher peak temperature and broader molten pool were determined in the weld with an increasing power ratio, attributed to the greater intensity of the core beam as visualised in Fg. 2. Furthermore, a more rapid change in the shape and magnitude of the temperature profile was observed through the depth direction when the power ratio increased, indicating that the ring beam is beneficial for stabilising the keyhole and maintaining a more uniform thermal field.

4.4. Effect of power ratio on weld grain structure

Due to the significant impact on weld mechanical performance, the grain structures of welds with different power ratios were investigated by combining the simulated thermal field results and the solidification principle. To demonstrate the evolution of solidification behaviour in transverse and depth directions, solidification parameters were studied along the molten pool boundary on the top surface and the
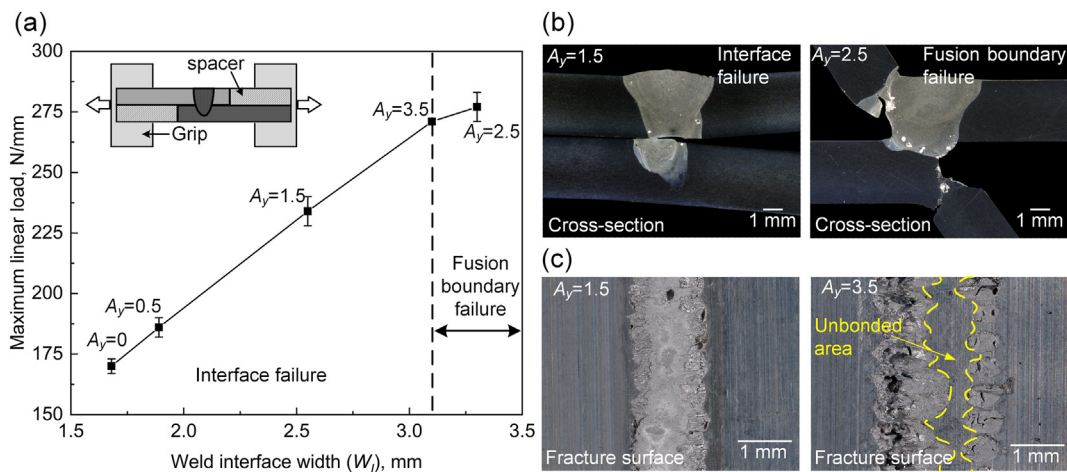
Fig. 5 − (a) Plot of the maximum linear load during tensile lap shear test as a function of weld interface width, (b) cross-section view of interface failure and fusion boundary failure, and (c) comparison of fractography in welds at $A_y = 1.5$ mm and $A_y = 3.5$ mm, showing the reduction of weld strength as a result of the unbonded region at excessive oscillation width.
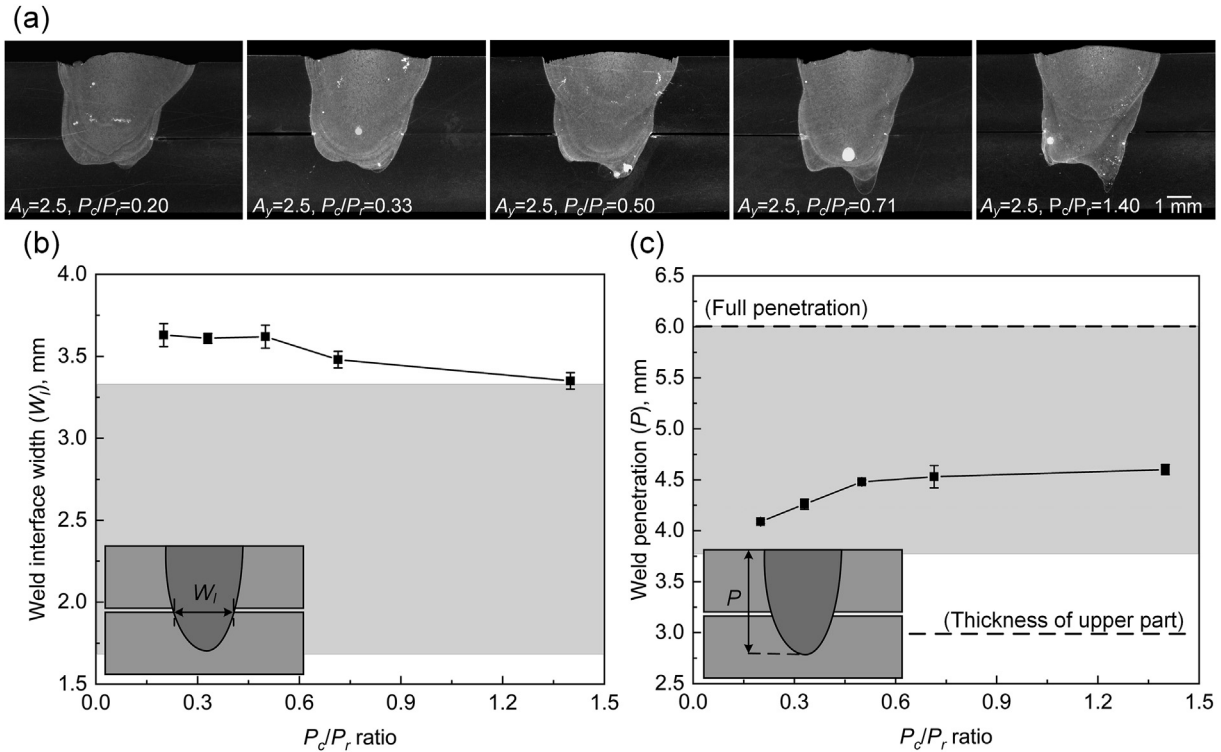
Fig. 6 — (a) Cross-section morphology of welds produced at different core/ring power ratios and evolution of weld geometry: (b) weld interface width (W_I) and (c) weld penetration (P). Note that the space highlighted in grey in (b) and (c) indicates the values obtained in the study of pre-selection of beam oscillation width (Fig. 4). Welding trials were conducted at the constant total power of 5.25 kW, power ratio of 1.63, oscillation frequency of 50 Hz and welding speed of 50 mm/s.
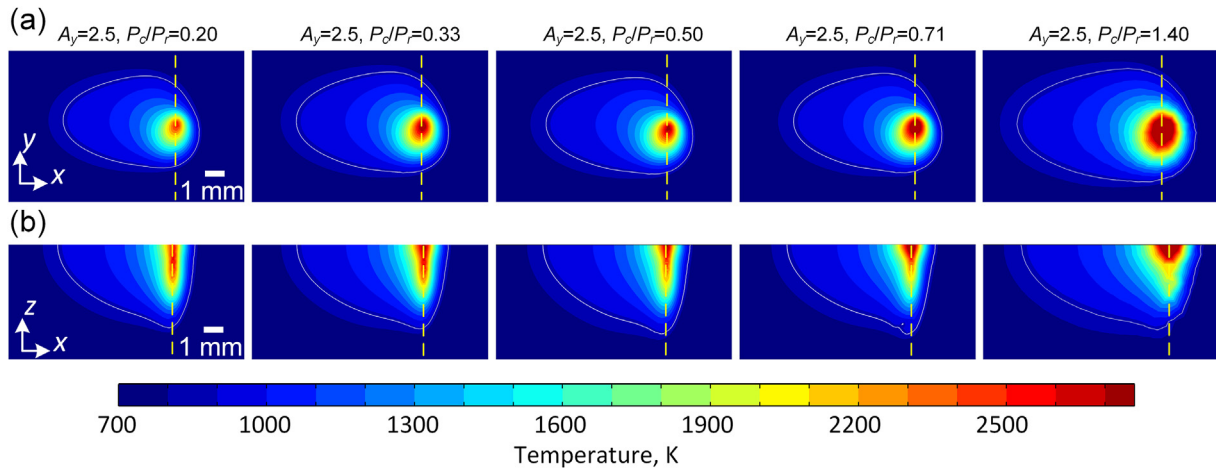
longitudinal cross-section at the weld centre, respectively (see Fig. 9). It has been proposed that the temperature gradient (G) and solidification rate (R) at the solidification front play a significant role in the grain formation during the solidification process, where G/R influences the grain morphology and G·R is associated with the scale of solidified microstructure [36]. It should be noted that welding trials in the pure ring beam (power ratio = 0) and pure core beam (power ratio = ∞) modes at an identical total power were also simulated to reveal the

evolution from the pure ring beam mode to the dual beam mode, which is not feasible by the experiment work yielded by the maximum power of the individual beam.

In the transverse direction, the G exhibits a relatively uniform distribution in the weld centre and increases rapidly towards the fusion boundary, Fig. 9(a). The G is determined to increase first from the power ratio of 0 (ring only) until the power ratio approaches 0.33 and then continuously drops as the power ratio increases. In comparison, the R decreases
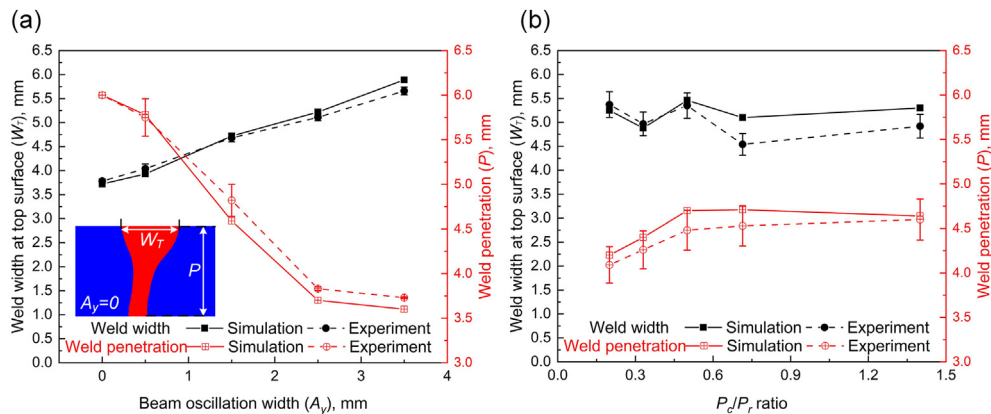

Fig. 7 — Comparison of weld profiles from simulation and experiment for welds produced with (a) various beam oscillation widths and (b) various core/ring power ratios. Note that the image embedded in (a) shows the fusion zone (in red) of the weld with $A_y = 0$ mm from the simulation.

Fig. 8 − Comparison of simulated steady-state temperature field in welds produced with different power ratios: (a) from the top surface (x-y plane) and (b) from a longitudinal cross-section along weld centre (x-z plane). Note that the dashed yellow lines indicate the position of the laser beam along the welding direction and solid white lines represent the molten pool boundary, expressed by the isothermal $(T_L + T_S)/2$ in the mushy zone. Detailed welding parameters are listed in Table 1.

from the weld centre towards the fusion boundary and only a slight difference was identified among welds with different power ratios except from the pure core beam mode Fig. 9(b). Consequently, the G/R follows a 'U' shape distribution with the minimum value located in the weld centre, Fig. 9(c). For aluminium alloy, a threshold value of G/R at approximate 7×10^3 ks/mm^2 was estimated over which the planar solidification occurs stably [37]. As the G/R values determined in all
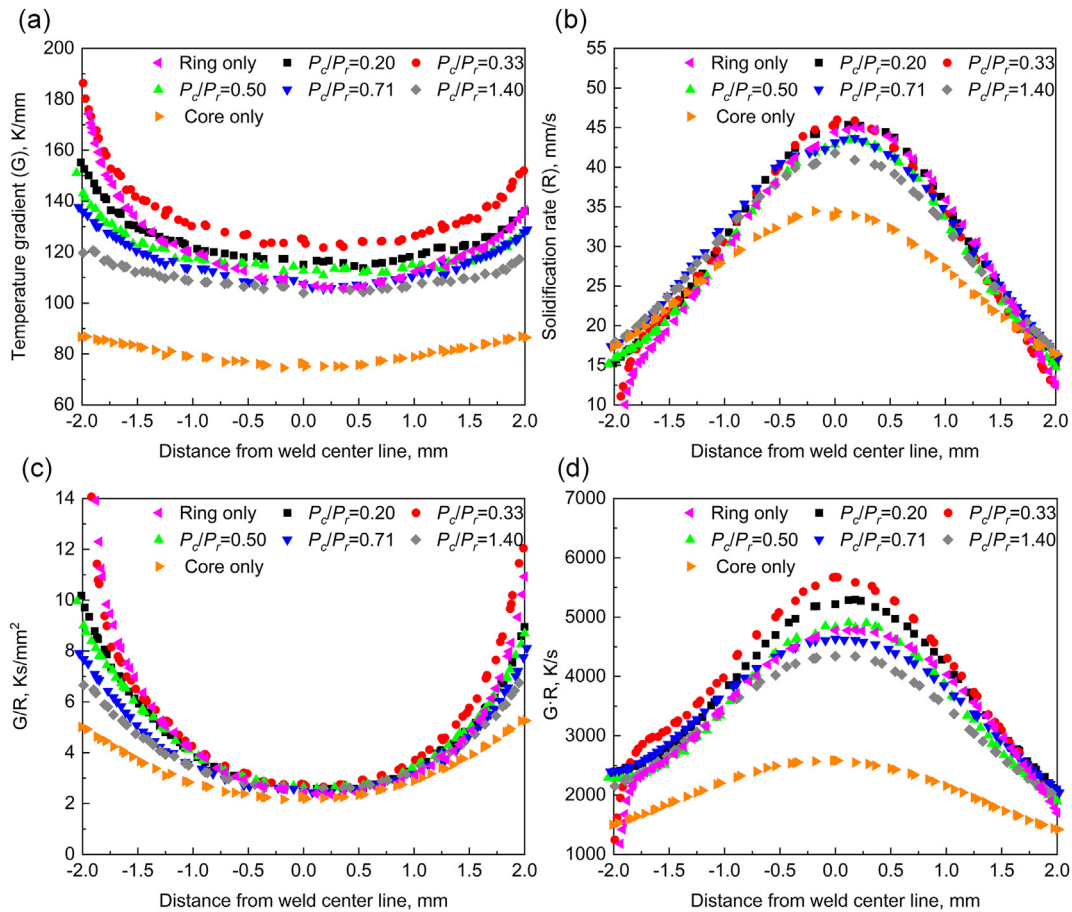
Fig. 9 − Comparison of the solidification parameters for welds produced with different power ratios, extracted from the simulated top surface isothermal $(T_L + T_S)/2$ within the mushy zone (Fig. 8(a)): (a) temperature gradient (G), (b) solidification rate (R), (c) G/R and (d) G·R.
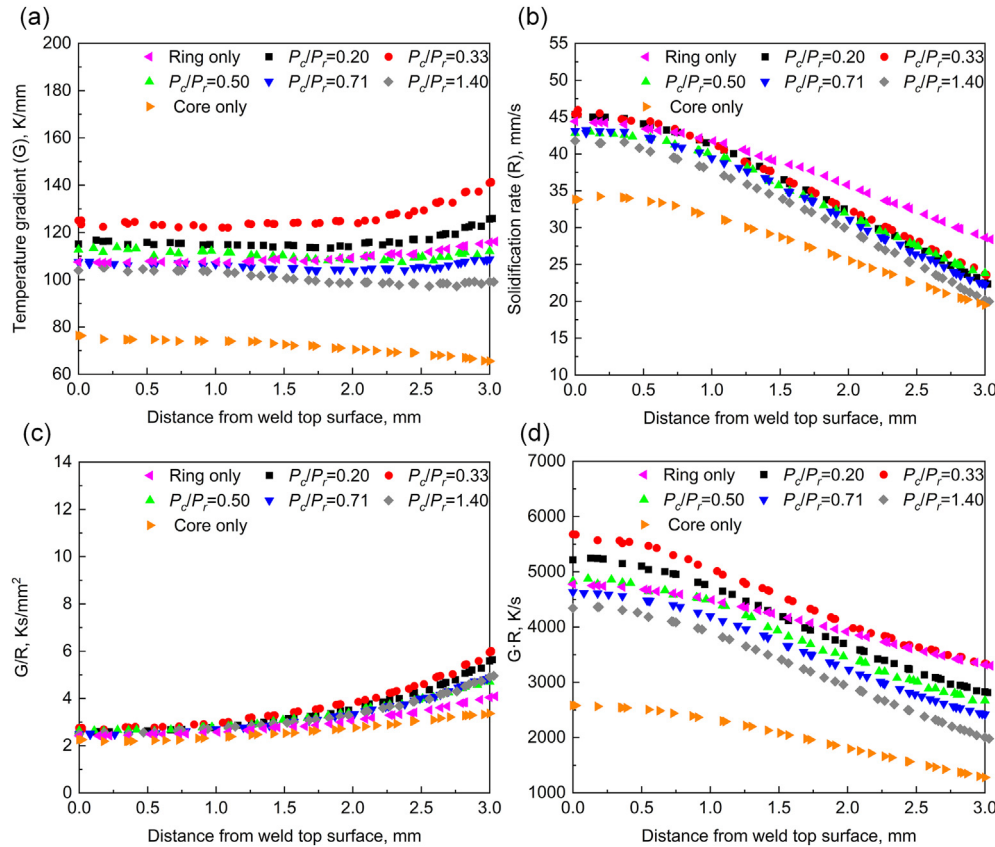
Fig. 10 — Comparison of the solidification parameters for welds produced with different power ratios, extracted from the simulated isothermal $(T_L + T_S)/2$ in the mushy zone on the longitudinal cross-section (Fig. 8(b)): (a) temperature gradient (G), (b) solidification rate (R), (c) G/R and (d) G·R.

welds here are apparently lower than this critical value, cellular or dendritic solidified microstructure is expected in the fusion zone. The cooling rate G·R (Fig. 9(d)) followed an inverted 'U' shape distribution with the peak value determined in the weld centre, indicating the refined grain structure in the weld centre and promoted grain growth towards the fusion boundary. As the power ratio increases from zero (ring-only mode), a parabolic distribution of the peak G·R is observed, with the highest value at the power ratio of 0.33. This could be explained by the combined impact of the ring beam and core beam as follows: At the extremely low power ratio, for example the ring only mode at the power ratio of zero, the ring provides excessive pre-heating and post-heating, promoting a mitigating thermal gradient and slowing down the cooling process. At the excessively high power ratio, for instance the core only mode (infinite power ratio), the excessive intensity of core beam results in a high peak temperature and a long time for heat dissipation prior to the occurrence of solidification, which consequently reduces the thermal gradient at the isothermal of $(T_L + T_S)/2$, and also lowers the cooling rate, as the temperature range for solidification moves towards the tail of the cooling curve. It is believed that the evolution of cooling rate is dominated by the ring beam at a low power ratio, for example, from 0 (ring only) to 0.33, where the ring beam has comparable intensity to the

core beam but a significantly larger affected area (see Fig. 2). In contrast, the core beam dominates the change of cooling rate at a high power ratio because of the higher beam intensity. Therefore, a balance associated with the highest cooling rate was determined at the power ratio of ~0.33 for the welding parameters employed in this study, which principally attributes to the most promising grain refinement.

In the depth direction, a uniform distribution of G is seen with a slight increase near the interface of two plates (depth = 3 mm), Fig. 10(a), and the R decreases as the depth increases, Fig. 10(b). Consequently, a sustained decline in cooling rate G·R is observed, Fig. 10(d), suggesting the increasing grain size from the top surface. Furthermore, the evolution of magnitudes of G, R, G/R and G·R as a function of the power ratio follows the same trend as seen in the transverse direction, Fig. (9).

EBSD analysis was performed across the weld zone on the transverse cross-section to quantitively investigate the impact of power ratio on the grain structure and validate findings obtained from the numerical simulation. Grain structure maps presented in Fig. 11 and the statistical grain size distribution in the fusion zone of the upper sheet, where the failure occurs during the tensile lap shear test, are shown in Fig. 12. Overall, the columnar grains grow from the fusion line towards the weld centre both transversely and vertically,
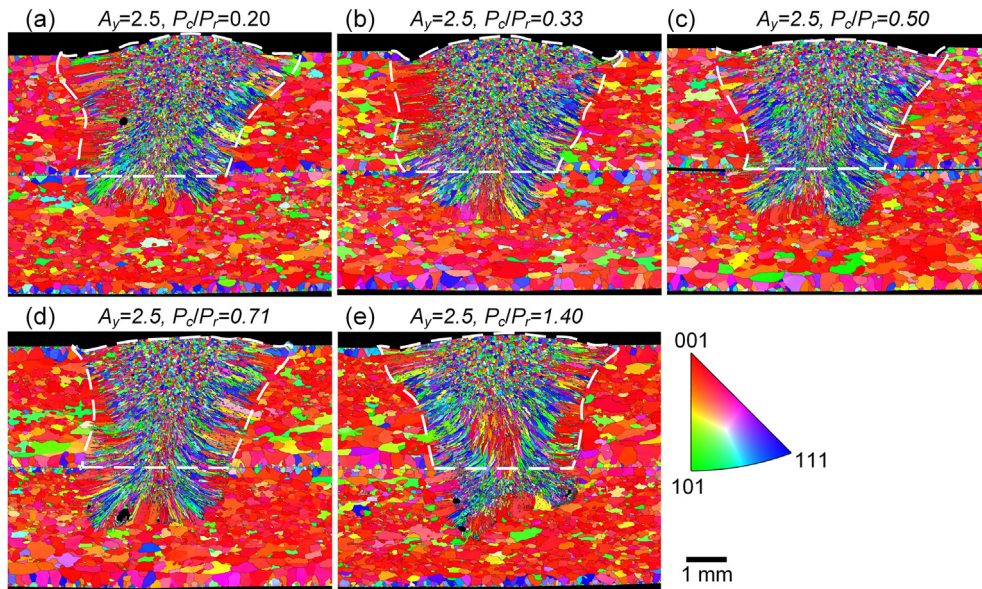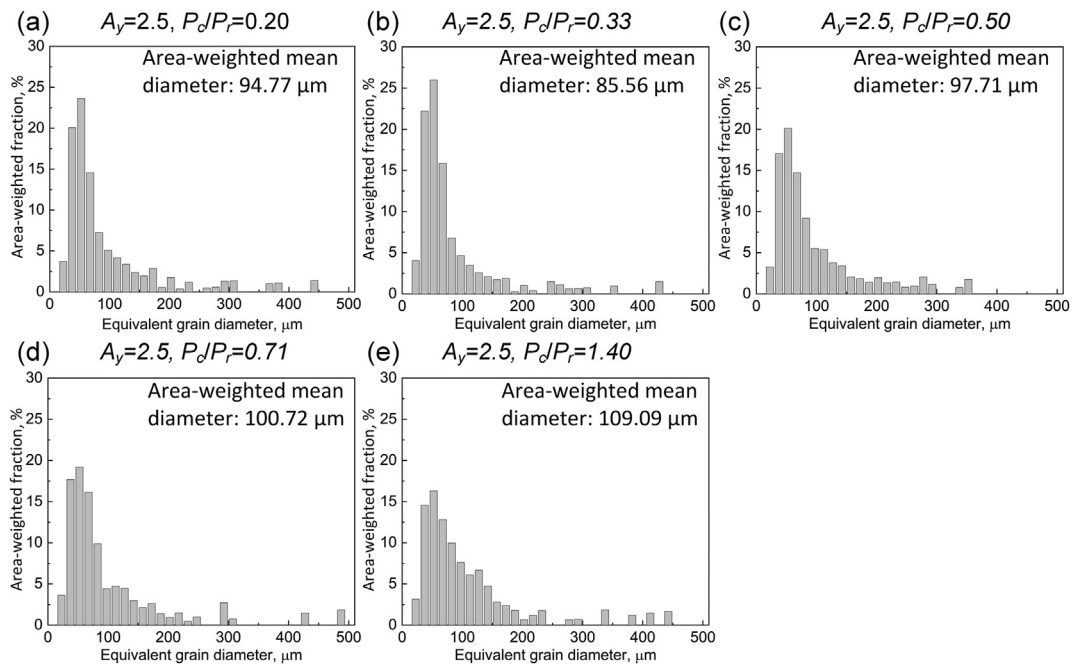
Fig. 11 — EBSD IPF maps showing the grain structures in welds produced with the power ratio of core to ring beam at (a) 0.20, (b) 0.33, (c) 0.5, (d) 0.71 and (e) 1.40. The dashed line indicates the region for the grain size distribution statistical analysis in Fig. 12 (fusion zone within the upper plate). Welding trials were conducted at the constant total power of 6.0 kW, oscillation width of 2.5 mm, oscillation frequency of 50 Hz and welding speed of 50 mm/s.

indicating the thermal gradient during the solidification process. In addition, a significant amount of fine equiaxed grains were observed in the weld centre because the beam oscillation results in a more uniform temperature distribution in the weld centre and resultantly wider constitutive undercooling region [14,38]. It is also evident from Fig. 11 that an increasing power ratio promotes the nucleation and growth of columnar grains near the interface between two plates. This can be statistically demonstrated by the more spread distribution of grain size in welds at a higher power ratio. For example, frequencies of grains finer than 50 μm are much reduced while frequencies of grains coarser than 100 μm gradually develop when comparing Fig. 12(e) with Fig. 12(b). It is believed that in the case of a high power ratio, the evolution of grain structure

Fig. 12 — Weld zone grain size distribution in welds produced with the power ratio of core to ring beam at (a) 0.20, (b) 0.33, (c) 0.5, (d) 0.71 and (e) 1.40, summarised from the fusion zone of upper part as indicated in EBSD maps, Fig. 11. Note that grain size is expressed by the equivalent diameter of the circle with an area equal to the grain.
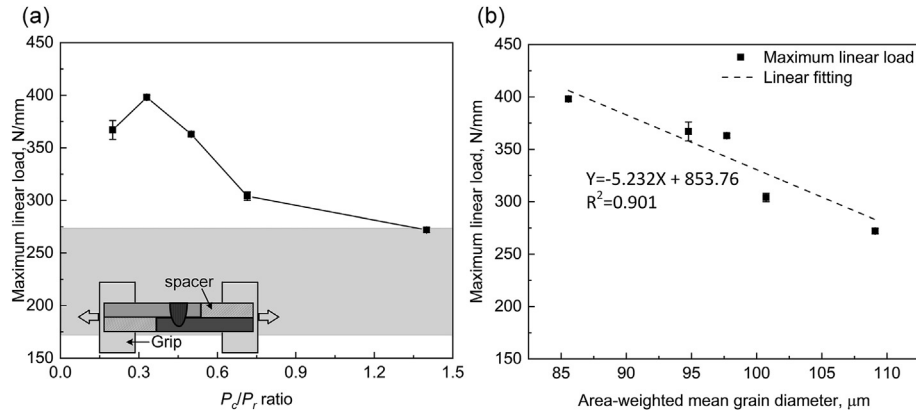
Fig. 13 – Plot of (a) the maximum linear load during tensile lap shear test as a function of core/ring power ratio (b) linear fitting between the maximum linear load and weld zone grain size. Note that the space highlighted in grey in (a) indicates the variation of maximum linear load in the study of oscillation width (Fig. 5). Welding trials were conducted at the constant total power of 6.0 kW, oscillation width of 2.5 mm, oscillation frequency of 50 Hz and welding speed of 50 mm/s.

in the depth direction is related to the sufficiently low cooling rate at the interface, which is observed to be comparable to the cooling rate at the fusion boundary (see Figs. 9(d) and Fig. 10(d)). Furthermore, the minimum area-weighted mean grain size and restricted formation of columnar grains near the interface in the weld with a power ratio of 0.33 are well correlated to the highest cooling rate, $G \cdot R$, in both transverse and depth directions, which confirms the reliability of the numerical simulation.

4.5. Effect of power ratio on weld mechanical performance

Fig. 13(a) plots the evolution of the mechanical strength of welds with different power ratios. Overall, the joint strength increases from ~275 N/mm to ~400 N/mm as the power ratio decreases, with the peak value captured at the power ratio of 0.33. It is interesting to see that the variation of joint strength resulting from different power ratios is more significant than
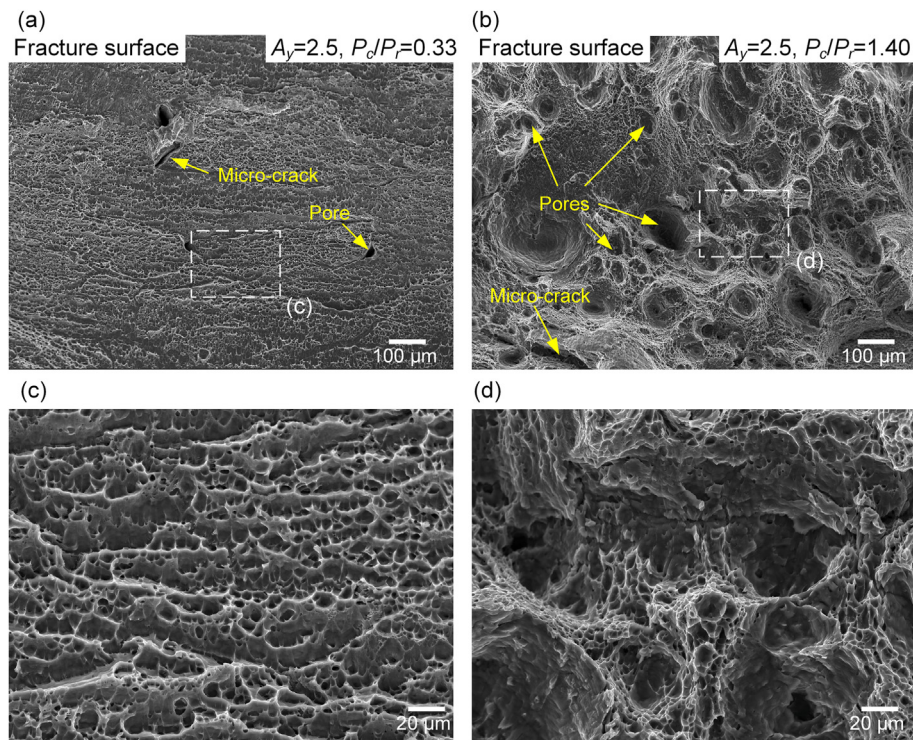
Fig. 14 – SEM fractography of welds produced at the power ratio of (a) 0.33 and (b) 1.40, after the tensile lap shear test, with failure determined in the fusion boundary. (c) and (d) are high magnification views of the area highlighted in (a) and (b), respectively. Representative microcracks and pores are highlighted by arrows.

in the cases with different oscillation widths, although the weld interface width remains comparable. In addition, fusion boundary failure was observed among all welds, confirming the findings in Fig. 5 that the weld interface width determines the failure mode. The linear correlation between the joint strength and area-weighted mean grain diameter, with $R^2 = 0.901$ in Fig. 13 (b), indicates that grain refinement is one of the primary mechanisms that lead to the improvement of joint strength when optimising the power ratio of the ARM laser beam.

Fig. 14 shows the fractography of welds produced at the power ratio of 0.33 and 1.40 after the tensile lap shear test, corresponding to the maximum and minimum joint strength. Uniform distribution of dimples was observed in the case with a power ratio of 0.33, with few pores and micro-cracks. In comparison, a much more frequent presence of pores and micro-cracks was captured in the weld produced at the power ratio of 1.40, which significantly reduces the resistant area and facilitates the rapid failure subjected to external tensile loading. Results indicate a more stable keyhole is expected during the welding processing with a lower power ratio. The direct observation of keyhole behaviour as a function of power ratio will be carried out in the future.

5.   Conclusions

This paper studied the impact of Adjustable-Ring-Mode (ARM) laser beam on the weld microstructure and mechanical performance of laser welded 6xxx aluminium alloy to explore the capability of new emerging laser technology for E-mobility manufacturing. A remote laser welding system equipped with transverse beam oscillation was employed and welding parameters, including the beam oscillation width and core/ring power ratio of the ARM laser beam, were investigated sequentially. A combination of experiments and FEM modelling have been presented to study weld geometry, fusion zone grain structure and weld mechanical strength, as well thermal evolutions within and around the weld. The FEM model provided information about temperature gradient and solidification behaviour, which are difficult to measure directly via experiments. The two main findings were summarised as follows:

The core/ring power ratio of the ARM laser beam at a constant total power has a limited control on the weld geometry when integrated with beam oscillation. Findings showed that increasing the beam oscillation width, up to 2.5 mm, tends to distribute the heat input across a wider area and, consequently, results in larger effective weld interface width. A threshold value of 3.1 mm (close to the plate thickness) was determined to activate the transition from interface failure to the fusion boundary failure subjected to tensile lap shear loading, leading to significant improvement in joint strength from 170 N/mm to 277 N/mm. Conversely, wider oscillation width, above 2.5 mm, turns to a significant reduction in energy density and results in significant reduction in the weld interface width and drop in joint strength, 270 N/mm.

Proper core/ring power ratio can restrict the formation of columnar grains near the interface between the two plates,

resulting in grain refinement within the weld zone. Extremely high power ratio, for example the core beam alone mode (infinite power ratio), results in high peak temperature and allows a long time for heat dissipation prior to solidification, leading to low thermal gradient and cooling rate at the solidification front; Extremely low power ratio, for example the ring beam along mode (zero power ratio), provides excessive pre-heating and post-heating, mitigating the thermal gradient and slowing down the cooling process. Results showed that a compromised solution which balances the wider formation of equiaxed dendrites and better grain refinement was determined at the power ratio of 0.33. This translated to the improvement in joint strength up to 400 N/mm.

The paper proved the feasibility of controlling the microstructure of laser welded 6xxx aluminium alloy by using ARM laser technology. This opens interesting future opportunities in the area of laser beam shaping as a tool to create bespoke microstructures, as well as control of phase formations and intermetallic during joining dissimilar materials.

Declaration of Competing Interest

The authors declare that they have no known competing financial interests or personal relationships that could have appeared to influence the work reported in this paper.

Acknowledgements

REFERENCES

[1] Meschke J, Tölle J, Berger L. Multi-material concept for a battery electric vehicle. ATZ Worldw 2017;119:48−53. https://doi.org/10.1007/s38311-017-0116-y.

[2] Mayyas A, Omar M, Hayajneh M, Mayyas AR. Vehicle's lightweight design vs. electrification from life cycle assessment perspective. J Clean Prod 2017;167:687−701. https://doi.org/10.1016/j.jclepro.2017.08.145.

[3] Ceglarek D, Colledani M, Váncza J, Kim DY, Marine C, Kogel-Hollacher M, et al. Rapid deployment of remote laser welding processes in automotive assembly systems. CIRP Ann − Manuf Technol 2015;64:389−94. https://doi.org/10.1016/j.cirp.2015.04.119.

[4] Erdos G, Kemény Z, Kovács A, Váncza J. Planning of remote laser welding processes. Procedia CIRP 2013;7:222−7. https://doi.org/10.1016/j.procir.2013.05.038.

[5] Zhao H, White DR, Debroy T. Current issues and problems in laser welding of automotive aluminum alloys. Int Mater Rev 1999;44:238–66. https://doi.org/10.1179/095066099101528298.

[6] Sun T, Franciosa P, Sokolov M, Ceglarek D. Challenges and opportunities in laser welding of 6xxx high strength aluminium extrusions in automotive battery tray construction. Procedia CIRP 2020;94:565–70. https://doi.org/10.1016/j.procir.2020.09.076.

[7] Sun T, Franciosa P, Liu C, Pierro F, Ceglarek D. Effect of micro solidification crack on mechanical performance of remote laser welded AA6063 fillet lap joint in automotive battery tray construction. Appl Sci 2021;11. https://doi.org/10.3390/app11104522.

[8] Alshaer AW, Li L, Mistry A. Effect of filler wire properties on porosity formation in laser welding of AC-170PX aluminium alloy for lightweight automotive component manufacture. Proc Inst Mech Eng Times Part B J Eng Manuf 2017;231:994–1006. https://doi.org/10.1177/0954405415578584.

[9] Hagenlocher C, Weller D, Weber R, Graf T. Reduction of the hot cracking susceptibility of laser beam welds in AlMgSi alloys by increasing the number of grain boundaries. Sci Technol Weld Join 2019;24:313–9. https://doi.org/10.1080/13621718.2018.1534775.

[10] Weller D, Bezençon C, Stritt P, Weber R, Graf T. Remote laser welding of multi-alloy aluminum at close-edge position. Phys Procedia 2013;41:164–8. https://doi.org/10.1016/j.phpro.2013.03.065.

[11] Mohan A, Ceglarek D, Auinger M. Numerical modelling of thermal quantities for improving remote laser welding process capability space with consideration to beam oscillation. Int J Adv Manuf Technol 2022;123:761–82. https://doi.org/10.1007/s00170-022-10182-7.

[12] Wang L, Gao M, Zhang C, Zeng X. Effect of beam oscillating pattern on weld characterization of laser welding of AA6061-T6 aluminum alloy. Mater Des 2016;108:707–17. https://doi.org/10.1016/j.matdes.2016.07.053.

[13] Fetzer F, Sommer M, Weber R, Weberpals JP, Graf T. Reduction of pores by means of laser beam oscillation during remote welding of AlMgSi. Opt Laser Eng 2018;108:68–77. https://doi.org/10.1016/j.optlaseng.2018.04.012.

[14] Li L, Gong J, Xia H, Peng G, Hao Y, Meng S, et al. Influence of scan paths on flow dynamics and weld formations during oscillating laser welding of 5A06 aluminum alloy. J Mater Res Technol 2020;11:19–32. https://doi.org/10.1016/j.jmrt.2020.12.102.

[15] Zhang C, Li X, Gao M. Effects of circular oscillating beam on heat transfer and melt flow of laser melting pool. J Mater Res Technol 2020;9:9271–82. https://doi.org/10.1016/j.jmrt.2020.06.030.

[16] Victor B, Kliner D, Hepp M. Is beam shaping the future of laser welding? Ind Laser Solut 2019;34(5):9–12.

[17] Rasch M, Roider C, Kohl S, Strauß J, Maurer N, Nagulin KY, et al. Shaped laser beam profiles for heat conduction welding of aluminium-copper alloys. Opt Laser Eng 2019;115:179–89. https://doi.org/10.1016/j.optlaseng.2018.11.025.

[18] Duocastella M, Arnold CB. Bessel and annular beams for materials processing. Laser Photon Rev 2012;6:607–21. https://doi.org/10.1002/lpor.201100031.

[19] Maina MR, Okamoto Y, Okada A, Närhi M, Kangastupa J, Vihinen J. High surface quality welding of aluminum using adjustable ring-mode fiber laser. J Mater Process Technol 2018;258:180–8. https://doi.org/10.1016/j.jmatprotec.2018.03.030.

[20] Mohammadpour M, Wang L, Kong F, Kovacevic R. Adjustable ring mode and single beam fiber lasers: a performance comparison. Manuf Lett 2020;25:50–5. https://doi.org/10.1016/j.mfglet.2020.07.003.

[21] Sokolov M, Franciosa P, Sun T, Ceglarek D, Dimatteo V, Ascari A, et al. Applying optical coherence tomography for weld depth monitoring in remote laser welding of automotive battery tab connectors. J Laser Appl 2021;12028:33. https://doi.org/10.2351/7.0000336.

[22] ISO EN. 6892–6901. Metallic materials-Tensile testing-Part 1: method of test at room temperature. Int Organ Stand 2009.

[23] Faraji AH, Maletta C, Barbieri G, Cognini F, Bruno L. Numerical modeling of fluid flow, heat, and mass transfer for similar and dissimilar laser welding of Ti-6Al-4V and Inconel 718. Int J Adv Manuf Technol 2021;114:899–914.

[24] Ai Y, Jiang P, Shao X, Li P, Wang C. A three-dimensional numerical simulation model for weld characteristics analysis in fiber laser keyhole welding. Int J Heat Mass Tran 2017;108:614–26. https://doi.org/10.1016/j.ijheatmasstransfer.2016.12.034.

[25] Bag S, Trivedi A, De A. Development of a finite element based heat transfer model for conduction mode laser spot welding process using an adaptive volumetric heat source. Int J Therm Sci 2009;48:1923–31. https://doi.org/10.1016/j.ijthermalsci.2009.02.010.

[26] Abderrazak K, Bannour S, Mhiri H, Lepalec G, Autric M. Numerical and experimental study of molten pool formation during continuous laser welding of AZ91 magnesium alloy. Comput Mater Sci 2009;44:858–66. https://doi.org/10.1016/j.commatsci.2008.06.002.

[27] Artinov A, Bachmann M, Rethmeier M. Equivalent heat source approach in a 3D transient heat transfer simulation of full-penetration high power laser beam welding of thick metal plates. Int J Heat Mass Tran 2018;122:1003–13. https://doi.org/10.1016/j.ijheatmasstransfer.2018.02.058.

[28] Shi L, Li X, Jiang L, Gao M. Numerical study of keyhole-induced porosity suppression mechanism in laser welding with beam oscillation. Sci Technol Weld Join 2021;26:349–55. https://doi.org/10.1080/13621718.2021.1913562.

[29] Mohan A, Ceglarek D, Auinger M. Effect of beam oscillation on the fluid flow during laser welding. Mater Today: Proceed 2022;59:1846–51. https://doi.org/10.1016/j.matpr.2022.04.435.

[30] Ribic B, Rai R, DebRoy T. Numerical simulation of heat transfer and fluid flow in GTA/Laser hybrid welding. Sci Technol Weld Join 2008;13:683–93. https://doi.org/10.1179/136217108X356782.

[31] Slováček M, Diviš V, Junek L, Ochodek V. Numerical simulation of the welding process — distortion and residual stress prediction, heat source model determination. Weld. World 2005;49:15–29.

[32] Geng S, Jiang P, Shao X, Guo L, Gao X. Heat transfer and fluid flow and their effects on the solidification microstructure in full-penetration laser welding of aluminum sheet. J Mater Sci Technol 2020;46:50–63. https://doi.org/10.1016/j.jmst.2019.10.027.

[33] Ltd. SS. JMatPro. 2014.

[34] Ma J, Kong F, Liu W, Carlson B, Kovacevic R. Study on the strength and failure modes of laser welded galvanized DP980 steel lap joints. J Mater Process Technol 2014;214:1696–709. https://doi.org/10.1016/j.jmatprotec.2014.03.018.

[35] Miyazaki Y, Furusako S. Tensile shear strength of laser welded lap joints. Nippon Steel Tech Rep 2007:28–34.

[36] Kou S. Welding metallurgy. 2003. p. 223–5. New Jersey, USA, 431.

[37] Geng S, Jiang P, Shao X, Mi G, Wu H, Ai Y, et al. Effects of back-diffusion on solidification cracking susceptibility of Al-Mg alloys during welding: a phase-field study. Acta Mater 2018;160:85–96.

[38] Jiang Z, Chen X, Li H, Lei Z, Chen Y, Wu S, et al. Grain refinement and laser energy distribution during laser oscillating welding of Invar alloy. Mater Des 2020;108195:186. https://doi.org/10.1016/j.matdes.2019.108195.